IEEE Access
Multidisciplinary | Rapid Review | Open Access Journal

Received January 8, 2020, accepted January 28, 2020, date of publication February 4, 2020, date of current version February 18, 2020.

Digital Object Identifier 10.1109/ACCESS.2020.2971563

Rotman Lens-Fed Antenna for Generating Multiple Orbital Angular Momentum (OAM) Modes With Gain Enhancement

DAN WU[1], ZHIYA ZHANG[1], GUANG FU[1], XIAOWEI SHI[2], (Senior Member, IEEE), LIN YANG[1], AND XI LI[1]

[1]Science and Technology on Antenna and Microwave Laboratory, Xidian University, Xi'an 710071, China
[2]School of Electronic Engineering, Xidian University, Xi'an 710071, China

Corresponding authors: Dan Wu (wudan44552@163.com) and Zhiya Zhang (zhiyazhang@163.com)

This work was supported in part by the National Natural Science Foundation of China under Grant 61601338, and in part by the National Natural Science Foundation of Shaanxi Province under Grant 2019JM-489.

ABSTRACT A compact multi-layer Rotman lens-fed array antenna which can generate nine orbital angular momentum (OAM) modes is presented in this paper. The proposed antenna consists of a microstrip Rotman lens and a nine-element circular array antenna which utilizes high-gain patch element in order to enhance the gain of OAM beam. A stacked patch loaded with two slots is attached above the patch element to effectively enhance the antenna gains. By employing the Rotman lens as the feed network of the circular array, nine OAM-carrying beams of modes number $\ell = 0, \pm1, \pm2, \pm3$ and ±4 can be produced when different input ports are excited, respectively. 160°-phase-shift on adjacent output ports can be achieved to meet the phase requirement of OAM modes of $\ell = \pm4$. Moreover, the Rotman lens is modified by adjusting the deflection angle of the beam ports and array ports so as to achieve uniform amplitude distribution on the output ports. Hence, the pattern characteristics of OAM beams can be effectively improved by making all the output ports are equal in amplitude. The C-band prototype of the antenna is fabricated and measured. Both the simulation and measurement results indicate that nine OAM modes can be generated by using the proposed structure. The proposed antenna can be used in an OAM-based wireless communication system.

INDEX TERMS OAM, Rotman lens, circular array antenna, high-gain antenna.

I. INTRODUCTION

Although the 1st version of the Fifth Generation New Radio standard (5G NR) has been completed by the Third Generation Partnership Project (3GPP) to meet the requirements set forth for IMT-2020 by the International Telecommunication Union (ITU), work on evolving wireless communication technologies is never stopped to fulfill the visions towards next generation. In particular, due to the continuous popularization of mobile internet and emerging immersive data services (e.g. AR/VR/hologram), the data demand is ever-growing and ultra-low latency is required, while spectrum is always limited, so drastic improvement on spectrum efficiency in parallel to exploit the new spectrum in high frequency bands could be envisioned towards 2030 (i.e. 6G era). The orbital angular momentum (OAM) technology, which would be one of the very effective means to improve channel capacity [1], [2], has attracted much attention rapidly in recent years. Intrinsically, electromagnetic (EM) waves can carry energy and angular momentum (AM) simultaneously but the latter one was rarely exploited for practical wireless communications in the past. The AM includes spin angular momentum (SAM) and orbital angular momentum, which describe the polarization state and the phase structure distribution, respectively [3]. OAM enables a new dimension for wireless data transmission and can be identified by the azimuthal phase distribution of $\exp(j\ell\varphi)$, where ℓ represents OAM mode and φ is the azimuthal angle. By encoding OAM mode ℓ, multiple information transmissions at the same frequency can be realized [4]. Therefore, to achieve an efficient OAM-based wireless communication system, antenna capable with high-order and multiple OAM modes are always in demand as prerequisite.

There have been many approaches proposed to generate OAM waves in literatures, such as spiral reflector in [5], planar-spiral phase plate (planar-SPP) in [6]–[8],

The associate editor coordinating the review of this manuscript and approving it for publication was Nagendra Prasad Pathak.

high-efficiency planar reflect arrays in [9], traveling-wave ring-slot structure in [10] and metasurface in [11], [12]. The study in [13] shows that vector antenna arrays can generate radio beams that exhibit OAM characteristics. Utilizing circular antenna array to achieve OAM beams can easily control the OAM modes and optimize the patterns, so it was widely studied [14]–[17]. The circular antenna array is also used in this paper for the generation of multiple OAM modes.

Although the methods listed above can generate good OAM modes, it is still a great challenge to realize multiple radiating waves with mutually independent OAM modes through a single aperture. In [18], half-mode substrate integrated waveguide antenna was proposed, which generated the OAM beams with four-OAM-mode. Based on metallic traveling-wave ring-slot structure, the OAM modes of $\ell = \pm 2$ and ± 3 was realized in [19]. In [20], helix antenna was firstly modified to radiate OAM wave, and the OAM modes of $\ell = 2$ and 3 was achieved. The metasurface using a ring-surrounded bowtie patch as a cell in [21] was adopted to generate multiple OAM modes of $\ell = 0$, 1 and 2. In [22] and [23], the circular antenna arrays with two feeding networks were employed to achieve two-OAM-mode radiation patterns. While only one phase-shifting feeding network was used in [24] to realize the OAM modes of $\ell = \pm 1$. Sequentially rotated configurations were adopted to generate circularly polarized OAM waves with OAM modes of $\ell = +1$ and $+2$ in [25]. In [26], a novel transmit array antenna which can achieve high gain and produce dual-mode OAM beams was proposed. The complex feeding network is the obstacle that restricts the circular antenna array to realize more higher-mode OAM waves.

In this paper, a well-designed Rotman lens is proposed as the feed of the circular antenna array to allow for lower complexity realization of multi-mode OAM antenna array. The circular antenna array consists of nine novel high-gain patch antennas. A stacked patch loaded with two slots is used on the patch element to effectively enhance the antenna gains. To generate even higher-order OAM mode of $\ell = \pm 4$ in this paper, the multiple-input and multiple-output Rotman lens is adopted to achieve an 160°-phase-shift among adjacent output ports. Moreover, the approach to improve the output amplitude distribution of Rotman lens is investigated for optimizing the performance of the OAM radiation patterns. Finally, we conclude by experiment results that the proposed antenna can effectively generate nine OAM modes of $\ell = 0$, ± 1, ± 2, ± 3 and ± 4.

II. NINE-OAM-MODE ANTENNA DESIGN

A. HIGH-GAIN ANTENNA ELEMENT

Fig.1 illustrates the configuration of the high-gain antenna element. It is composed of two layers of patches and a ground plane. As shown in Fig.1 (a), the stacked patch is printed on the top surface of the upper substrate, which has a relative permittivity of $\varepsilon_r = 2.65$ and a thickness of 0.5mm. Two slots with the same size are loaded on the stacked patch.

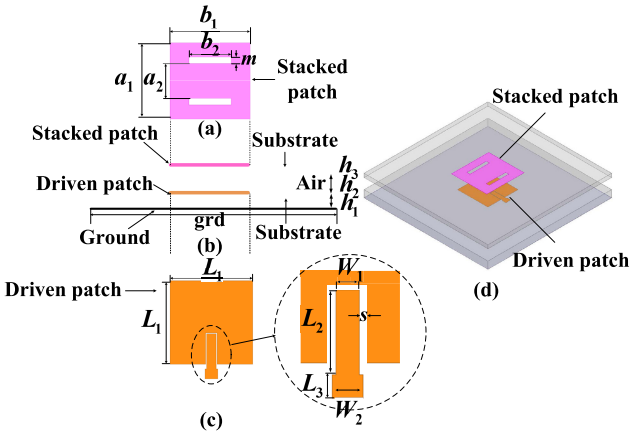

FIGURE 1. Geometry of the antenna element. (a) Upper stacked patch. (b) Side view. (c) Driven patch. (d) Perspective view.

The distance between the two slots is a_2 and the width of the slot is m. As is shown in Fig.1 (c), the driven patch with a side length of L_1 is fabricated on the top surface of the lower substrate which has a permittivity of $\varepsilon_r = 2.65$ and a thickness of 1mm. Foam clinker (ROHACELL 51 IG/A) with a permittivity of 1.07 and a loss tangent of 0.0003 is used between two layers to support the upper layer instead of air. The driven patch is coupling fed by a microstrip line through a U-shaped gap with a width of s, which is shown in Fig 1(c). The end of the microstrip line is connected to the feeding probe. In subsequent array designs, the end of the microstrip line is extended and connected to the lens through a metalized via holes. The ground plane is printed on the bottom surface of the lower substrate.

According to the Huygens' principle, the stacked patch can be considered as the four radiating slots with equivalent magnetic currents [27], [28]. The E-plane far-field radiated by the two slots at two sides can be derived as below [27]

$$E_{\theta 1} = C_1 \sin c(\pi h \sin\theta/\lambda)\cos(\pi a_1 \sin\theta/\lambda) \approx C_1 \cos(\pi a_1 \sin\theta/\lambda) \quad (1)$$

$$C_1 = j\frac{2a_1 V_1 e^{-jkr}}{\lambda r} \quad (2)$$

where h is the distance between the stacked patch and the ground, λ is the free-space wavelength, k is the propagation constant, V_1 is the voltage across the slot, and r is the distance from the far-zone point to the center of the patch.

The two loaded slots can be regarded as binary arrays of equal amplitude and phase, and the E-plane far-field radiated by them can be derived by the same method as above.

$$E_{\theta 2} = C_2 \sin c(\pi h \sin\theta/\lambda)\cos(\pi a_2 \sin\theta/\lambda) \approx C_2 \cos(\pi a_2 \sin\theta/\lambda) \quad (3)$$

$$C_2 = j\frac{2a_2 V_2 e^{-jkr}}{\lambda r} \quad (4)$$

where V_2 represents the amplitude of the two slots voltage.

It can be known from Fig. 2(a) that the stacked patch works in the TM01 mode with an electrical wall in the middle.

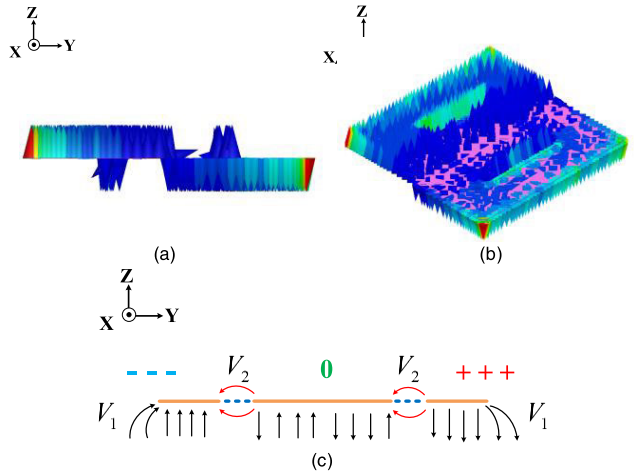

FIGURE 2. Electric field distribution of the proposed antenna: (a) Side view. (b) Perspective view. (c) Field distribution beneath the patch with two slots.

The voltage on the right side of the patch is positive, the left side is negative, and the voltage at the middle electrical wall is zero. The electric field on the loaded slot points from positive voltage to zero voltage, and then from zero voltage to negative voltage [28]. Therefore, the electric fields in the two loaded slots point in the -y direction, which is opposite to the electric field directions in the slots on both sides of the patch, as is shown in Fig. 2(c). The phase of the loaded slot is opposite to that of the other two slots. According to the principle of electric field superposition, the total far-field from the stacked patch can be obtained as.

$$\begin{aligned} E_{\theta T} &= E_{\theta 1} + E_{\theta 2} \\ &= C_1[\cos(\pi a_1 \sin\theta/\lambda) + \alpha\cos(\pi a_2 \sin\theta/\lambda)e^{j\beta}] \\ &= C_1[\cos(\pi a_1 \sin\theta/\lambda) - \alpha\cos(\pi a_2 \sin\theta/\lambda)] \quad (5) \\ \alpha &= C_2/C_1 \quad (6) \end{aligned}$$

where α and β are the amplitude ratio and phase difference of the electric field between the two loaded slots and the other two slots, respectively.

When the size of the two loaded slots are determined, α can be regarded as a constant. The E-plane radiation patterns of the stacked patch with $a_1 = 0.36\lambda$ are calculated under different value of a_2, as is shown in Fig. 3(a). It indicates that the beamwidth of the E-plane radiation patterns is effectively reduced by decreasing the slots spacing. Therefore, the radiation directivity of the whole antenna is improved by this method. The analysis above is verified in Fig. 3(b), which shows the radiation performance of the proposed antenna design with different value of a_2. However, the radiation efficiency of the antenna declines along with the decrease of the variable a_2 from 18mm to 2mm. To obtain the maximum gain of the antenna with given consideration of radiation efficiency, $a_2 = 9.2mm$ is finally selected.

In order to demonstrate the effect of the stacked patch, the three-stage structures of the antenna are depicted in Fig.4:

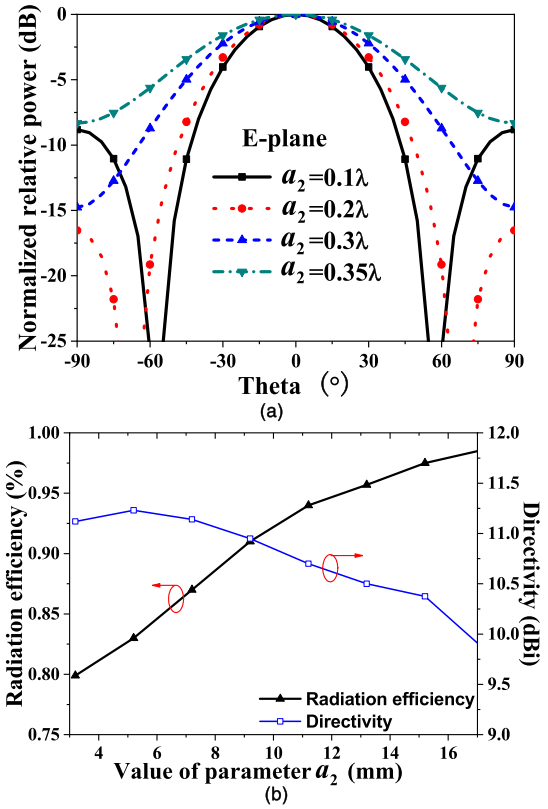

FIGURE 3. (a) E-plane radiation patterns (b) Radiation performance of the proposed antenna under the different value of a_2.

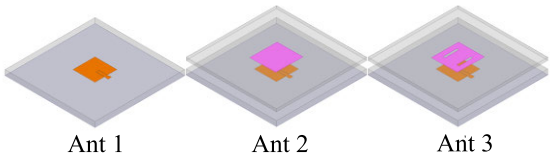

FIGURE 4. Three improved prototypes of the proposed antenna element.

Ant 1 is a rectangular microstrip antenna; A stacked patch is added in Ant 1 to realize Ant 2; Ant 3 is the proposed antenna which loads two slots on the stacked patch. The ground plane in simulation is assumed to be infinite. Fig. 5(a) shows the simulated E-plane radiation patters of the three antennas. It is noted that the directivity of the antenna is better after the stacked patch is added. Ant 3 adds two slots to Ant 2, which can further improve the directivity of the antenna from 10.1 dBi to 11.2 dBi. Hence, with the evolution of antenna from Ant 1 to Ant 3, the beamwidth in E-plane becomes narrower and the directivity is getting better.

Fig. 5(b) shows the simulated reflection coefficient of the proposed antenna element. Fig. 6 shows the simulated E- and H-plane patterns at 5.4GHz. The realized gain of the proposed antenna is 10.9dBi, and the half-power beamwidths (HBPW) of the E- and H-plane are 38.7° and 63.2°, respectively. The final dimensions of the antenna element are given in table 1. Comparison of the gain with other similar antennas is

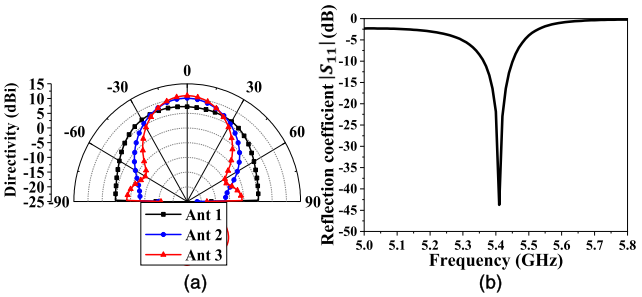

FIGURE 5. (a) Simulated E-plane radiation patterns for Ant 1, Ant 2 and Ant 3. (b) Simulated reflection coefficients of Ant 3.

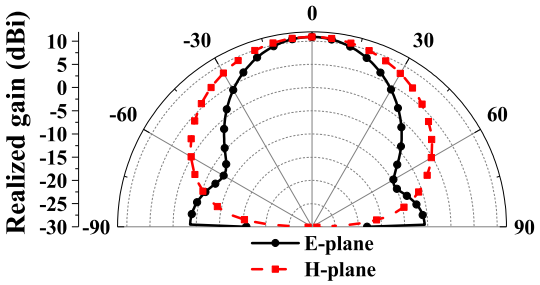

FIGURE 6. Radiation patterns of the proposed antenna.

TABLE 1. Design parameters of the proposed array element.

Design parameters	L_1	L_2	L_3	W_1	W_2	a_1	a_2
Value(mm)	17.1	7.2	2	2	2.65	20	9.2
Design parameters	b_1	b_2	grd	h_1	h_2	h_3	S
Value (mm)	21	11	70	1	4.1	0.5	0.2

TABLE 2. Comparison of the gain with other similar antennas.

Ref.	Antenna type	Freq. (GHz)	Dimensions	Gain (dBi)
[29]	Patch antenna	2.5	0.41 λ *0.41 λ *0.11 λ	9.7
[30]		2.9	0.61 λ *0.61 λ *0.03 λ	10.6
[31]		5.8	0.72 λ *0.72 λ *0.61 λ	10.2
[32]		4.2	0.84 λ *0.84 λ	12.8
[33]		4.0	1 λ *1 λ *0.05 λ	14.4
This work		5.4	0.38 λ *0.38 λ *0.1 λ	10.9

shown in table 2. The proposed antenna design shows good performance in terms of antenna gain without increasing the antenna dimensions.

B. DESIGN OF ROTMAN LENS

The Rotman lens has the characteristics of multi-input multi-output and symmetrical structure. Using the characteristics of Rotman lens, various output phase differences can be realized. Thus, multiple OAM modes are generated by using the Rotman lens as the feeding network.

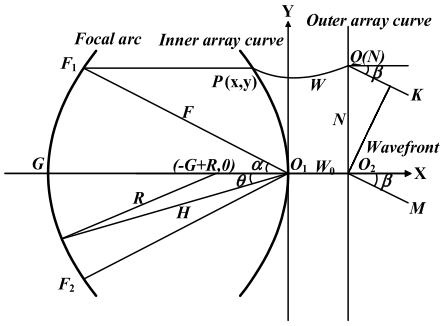

FIGURE 7. Geometry and design parameters of a Rotman lens.

The typical geometry and design parameters are shown in Fig. 7. The proposed Rotman lens is designed based on geometrical-optical (GO) theory, which is given by (7).

$$\begin{aligned} \overline{F_1P}\sqrt{\varepsilon_r} + W + N\sin\beta &= \sqrt{\varepsilon_r}F + W_0 \\ \overline{F_2P}\sqrt{\varepsilon_r} + W - N\sin\beta &= \sqrt{\varepsilon_r}F + W_0 \\ \overline{GP}\sqrt{\varepsilon_r} + W &= \sqrt{\varepsilon_r}G + W_0 \end{aligned} \tag{7}$$

where $\overline{F_1P}$, $\overline{F_2P}$, and $\overline{GP}$ are the path lengths from focal points F_1, F_2 and G, respectively, to the point P on the inner array curve, ε_r is the permittivity of the lens cavity.

To generate the higher-order OAM mode of $\ell = \pm 4$, the proposed Rotman lens is required to achieve an 160°-phase-shift among output ports. The scanning angle part of the parameters is substituted with phase difference in designing the lens. The position of the ports and the contours of the lens can be determined according to a series of parameters and equations, which were initially derived in [34]. It should be pointed out that the selection of the off-axis focal length F should be specially considered when designing the contours of the lens. The amplitude distribution of the output ports is significantly affected by off-axis focal length F. When the circular array is fed with unequal amplitude (The feeding amplitudes of the nine elements are 0.3, 0.5, 0.7, 1, 1, 1, 0.7, 0.5 and 0.3 respectively.), beam sag appears in the radiation patterns, as is shown in Figs. 8. This phenomenon exists especially in higher-order OAM radiation pattern. The difference in output amplitude is even worse when the terminal port of the Rotman lens is excited. Therefore, improving the performance of the output amplitude distribution is essential when using Rotman lens as a feeding network to generate high-order OAM modes.

Fig. 9 shows the contours of the lens under different values of F. With the decrease of F, the size of the lens decreases while the bending degree of the array curve increases. The dashed lines in the figure are equivalent electric field distribution curves in the lens when the terminal port B9 is fed. It can be clearly found that when the bending degree of the array curve becomes large, energy is difficult to transmit to port A9. This will result in the amplitude of port A9 being much smaller than that of other ports. The size and the loss of the lens will increase when the off-axis focal length F is too large. Considering the output port amplitude and the loss

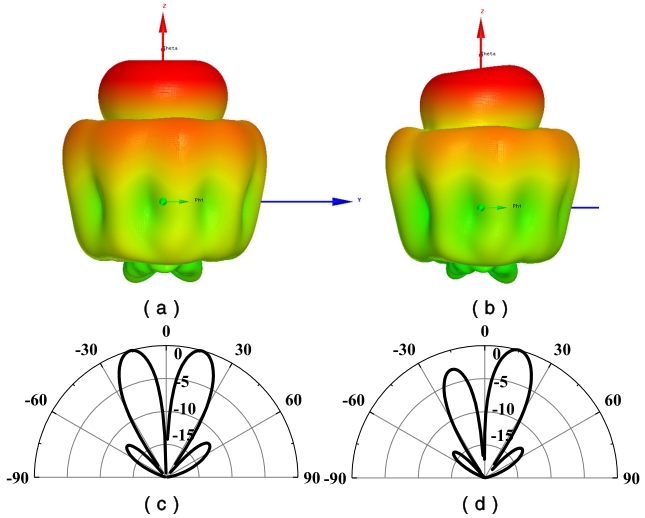

FIGURE 8. Radiation patterns of OAM mode $\ell = +1$. 3-D pattern fed with (a) equal and (b) unequal amplitude. Phi=90° plane radiation patterns fed with (c) equal and (d) unequal amplitude.

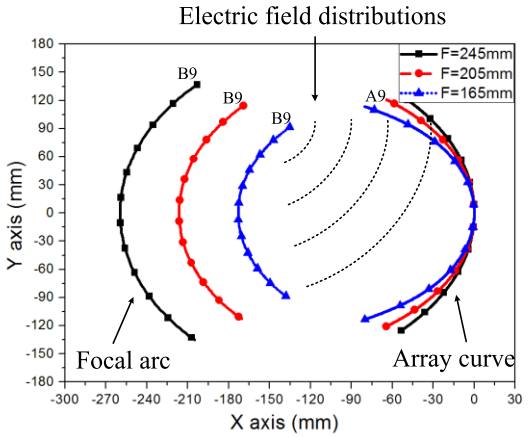

FIGURE 9. Contours of the lens under different values of F.

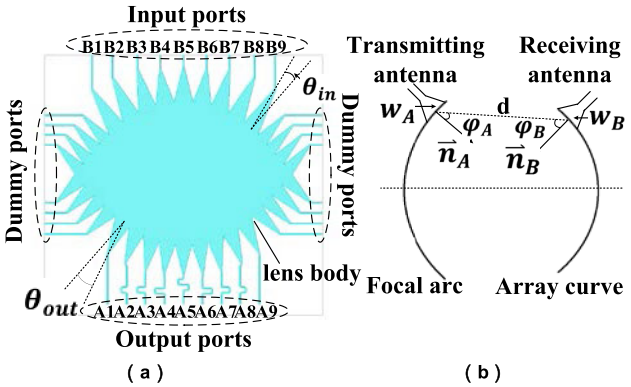

FIGURE 10. (a) Geometry of the Rotman lens. (b) Schematic diagram of equivalent aperture of the Rotman lens.

of the lens, the off-axis focal length of F =245mm is finally determined.

To further consider the amplitude of the output port, the deflection angles of the input port and the output port are analyzed respectively. The port deflection angle $\theta_{in}(\theta_{out})$

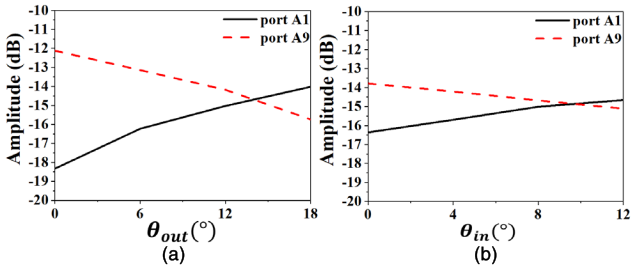

FIGURE 11. (a) results under different value of θ_{out}. (b) results under different value of θ_{in}.

is defined as the angle at which the port deviates from the center position as shown in Fig. 10(a). To theoretically analyze the transmission characteristics of the Rotman lens, both the input port and the output port are equivalent to a plane antenna with uniform aperture field distribution. As is shown in Fig. 10(b), the input and output port are equivalent to a transmitting antenna and a receiving antenna respectively, and the lens body is equivalent to a two-dimensional field region. Vectors $\overrightarrow{n_A}$ and $\overrightarrow{n_B}$ indicate the port orientations of the input and output ports, respectively. When the port position, port direction and port size are determined, the energy directly coupled between the input and output ports can be obtained according to the two-dimensional equivalent formula of Friis transmission equation.

$$S_{AB} = \frac{(2\pi w_A w_B/kd)^{\frac{1}{2}}}{\lambda}\left[\frac{\sin(\pi w_A \sin\varphi_A)/\lambda}{\pi w_A \sin\varphi_A/\lambda}\right]\cos(\varphi_A) \times\left[\frac{\sin(\pi w_B \sin\varphi_B)/\lambda}{\pi w_B \sin\varphi_B/\lambda}\right]\cos(\varphi_B)e^{-jkd} \quad (8)$$

where φ_A and φ_B respectively represent the included angle between the port direction of the input and output ports and the receiving direction of the output port.

Increasing variables θ_{in} and θ_{out} is equivalent to reducing φ_A and φ_B. Thus, the energy S_{AB} received by the output port becomes large, which can be obtained from equation (8). With the use of the above principle, the output amplitude distributions of the Rotman lens are effectively improved.

According to the characteristics of the Rotman lens, when the symmetrical ports B1 or B9 are fed, the amplitude difference between the output ports is the largest through simple analysis. Fig. 11(a) shows the amplitudes of ports A1 and A9 vary with the variation of θ_{out} when port B1 is excited. It is noted that when θ_{out} increases from 0° to 16°, the amplitude of port A1 increases while that of port A9 decreases gradually. Fig. 11(b) shows that when port B1 is fed, the amplitudes of ports A1 and A9 vary with the variation of θ_{in}. When θ_{in} increases from 0° to 12°, the amplitude of port A1 increases and that of port A9 decreases. To make the amplitudes of ports A1 and A9 are approximately in equal, $\theta_{out} = 12°$ and $\theta_{in} = 8°$ are finally selected. Hence, the amplitude distribution of Rotman lens can be improved by adjusting the deflection angles of ports. The characteristics of the other

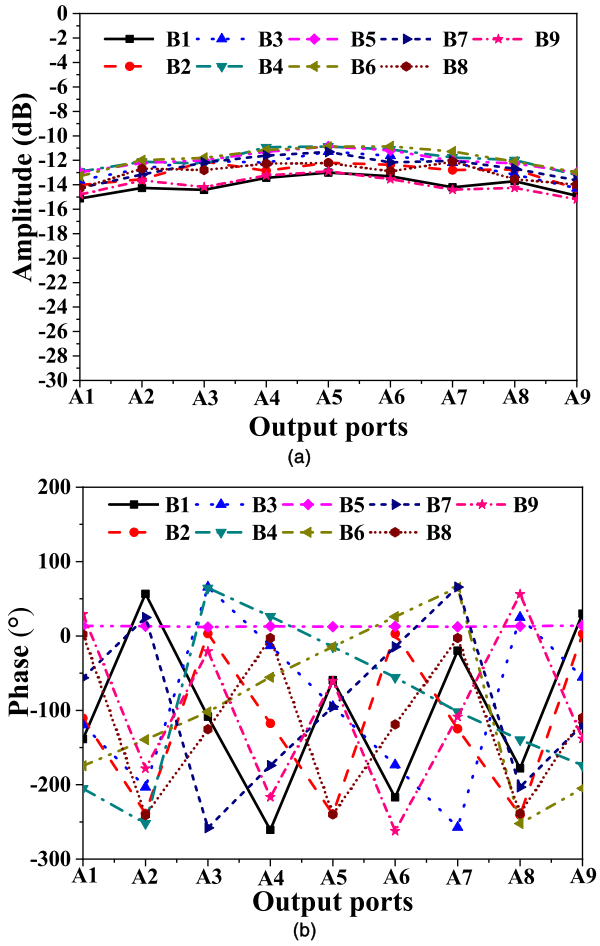

FIGURE 12. Performance of the Rotman lens. (a) Amplitudes. (b) Phases.

TABLE 3. Design parameters of the proposed Rotman lens.

Design parameters	Values
Design Frequency	5.4GHz
Maximum phase difference	160°
Ratio of focal length(g)	1.06
Off-axis focal length(F)	245mm
Substrate	$\varepsilon_r = 2.65$, t=1mm, $\tan\delta = 0.002$

ports can also be improved by this method to achieve equal amplitude distribution on the output ports of the Rotman lens.

Having discussed above, the Rotman lens final design is shown in Fig. 10(a), which consists of nine input ports, nine output ports, sixteen dummy ports and a lens body. Parameters of the Rotman lens are given in Table 3. Fig. 12(a) and (b) present the amplitude and phase distribution of the nine output ports at 5.4 GHz when each input port is excited. As shown in Fig. 13, each output port has a small amplitude difference, and the maximum amplitude difference is less than 3dB. As is shown in Fig. 12, the phase differences of 0°, ±40°,±80°, ±120° and ±160° are realized when each input port is excited, respectively. The detailed results of Rotman lens are summarized in Table 4.

TABLE 4. Detail results of the proposed Rotman lens.

Input port	Amplitude(dB) Max.	Amplitude(dB) Min.	phase differences(°)	Insertion loss(dB)
B1	-13	-15.1	-164.9~-152	3.4
B2	-12.1	-14.3	-127.7~-115.8	3.8
B3	-11.3	-14.2	-91.2~-77.8	4.1
B4	-10.9	-13.1	-46.1~-34.4	4.3
B5	-10.9	-13.0	-1.2~1.1	4.3
B6	-10.9	-13.3	35~47.3	4.4
B7	-11.3	-14.2	78.6~91.1	4.1
B8	-12.1	-14.3	115.4~128.6	3.8
B9	-12.9	-15.1	153.5~165.7	3.4

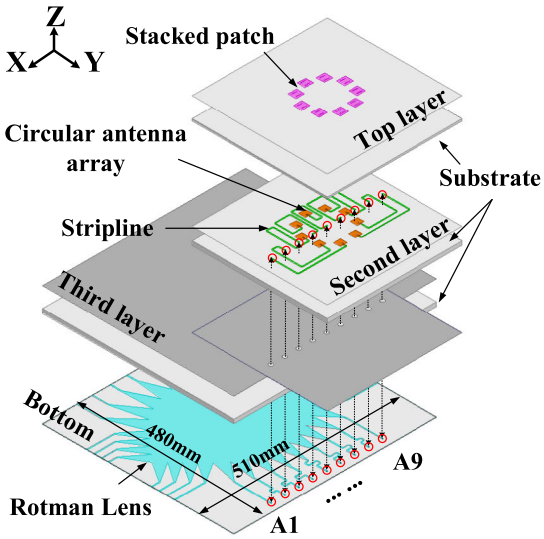

FIGURE 13. Geometry of the proposed multiple OAM modes antenna.

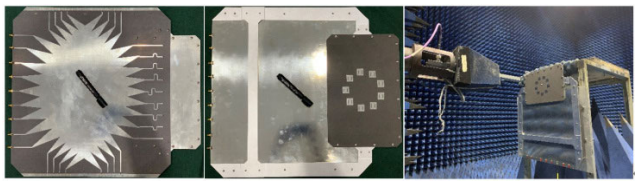

FIGURE 14. Photographs of the prototype and anechoic chamber.

C. REALIZATION OF MULTIPLE OAM MODES AND GEOMETRY OF THE NINE-OAM-MODE ANTENNA

The conventional circular array can be applied for OAM-generating by changing the excitation phase [1]. In this work, as shown in Fig. 13, a nine-element circular array is designed for generating nine OAM modes, and the array element adopts the high-gain microstrip antenna proposed in Section A. When the phase difference between the array elements is 0°, ±40°, ±80°, ±120° and ±160°, OAM with modes of $\ell = 0$, $\ell = \pm 1$, $\ell = \pm 2$, $\ell = \pm 3$ and $\ell = \pm 4$ can be generated, respectively. In order to make OAM

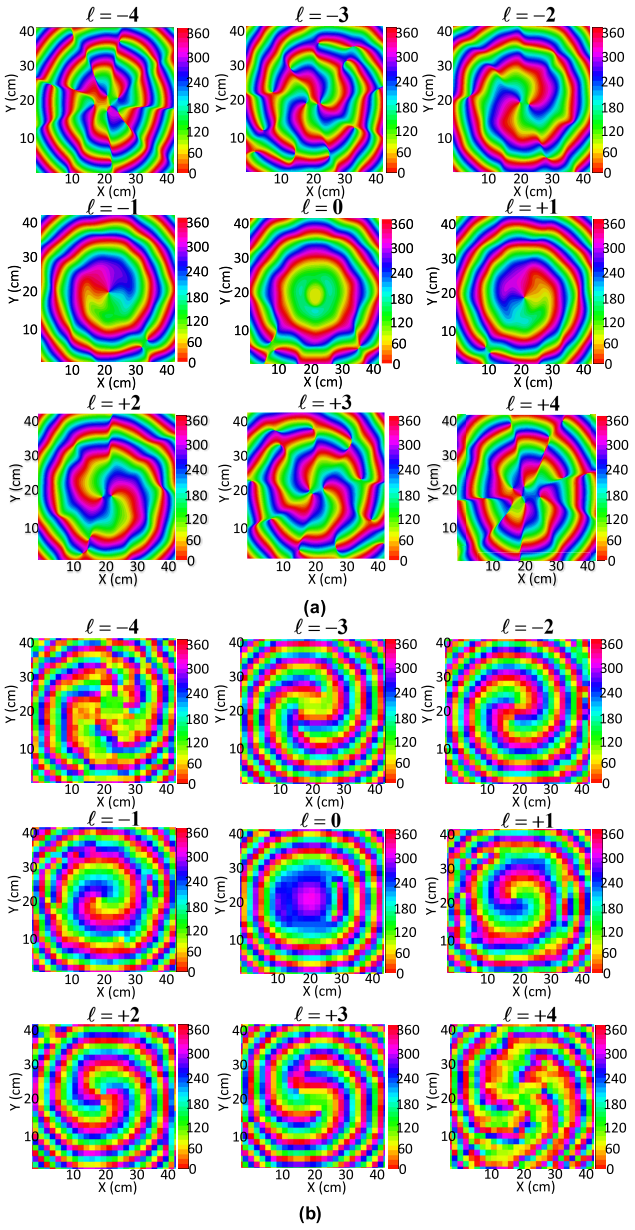

FIGURE 15. Simulation and measurement results of transverse phase patterns: (a) simulation results; (b) measurement results.

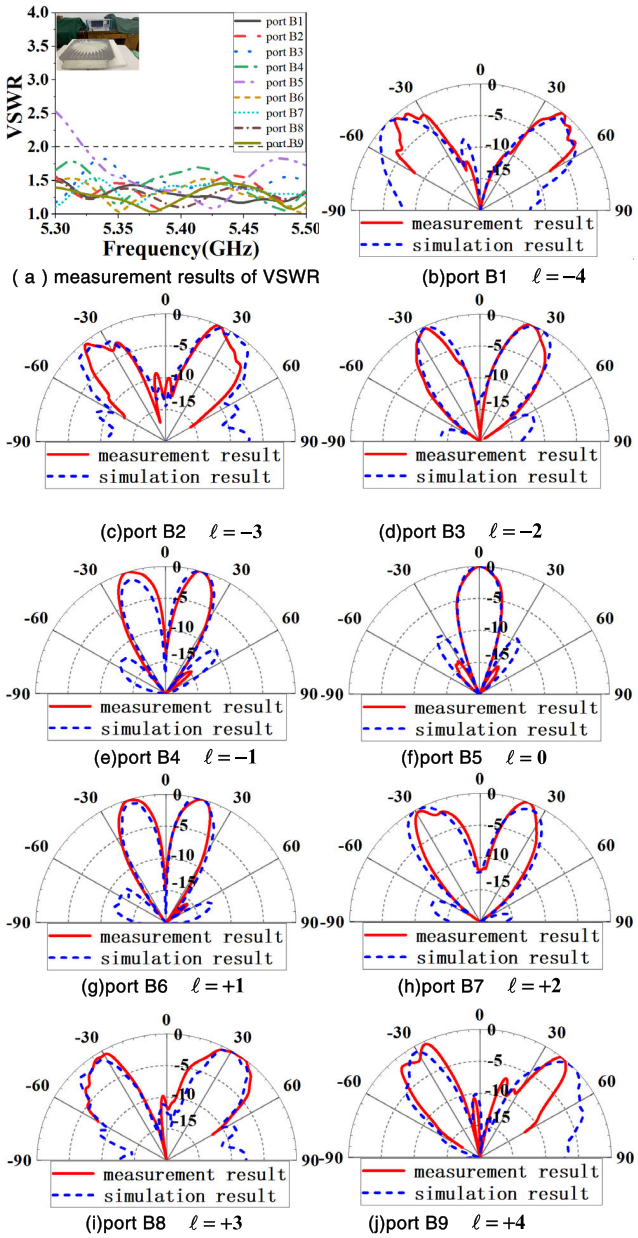

FIGURE 16. VSWR and far-field radiation patterns.

practically implementable, Rotman Lens proposed in section B can replace the traditional complex feeding network of multi-mode OAM antenna array, acting as the feed network and produce necessary phase shift for the circular array.

Fig. 13 shows the overall structure of the nine-OAM-mode antenna. The antenna is divided into four layers of patches, which are printed on three dielectric plates. The top two layers of patches are a nine-element circular array composed of nine high-gain elements which is described in Section A. Nine additional microstrip lines were added to the second layer to connect the Rotman lens and the circular array. The third layer is the common ground shared by the radiation patch and the Rotman lens. The bottom layer is a 9×9 Rotman lens. The outputs of the lens are connected with the microstrip lines on the second layer through nine metalized via holes through the common ground. The dimensions of the Rotman lens are shown in Fig. 13, and the final form factor of the proposed antenna design is 510mm × 570mm × 6.6mm.

III. EXPERIMENT RESULTS AND DISCUSSIONS

A prototype has been fabricated as shown in Fig. 14 (a) and (b) for the proof of the proposed design. Fig. 14(c) shows the measured status in anechoic chamber. Fig. 15(a) and (b) show respectively the simulated and measured electric field phase profiles for $\ell = 0, \pm1, \pm2, \pm3$ and ±4. The simulation and measurement results of the phase distribution are

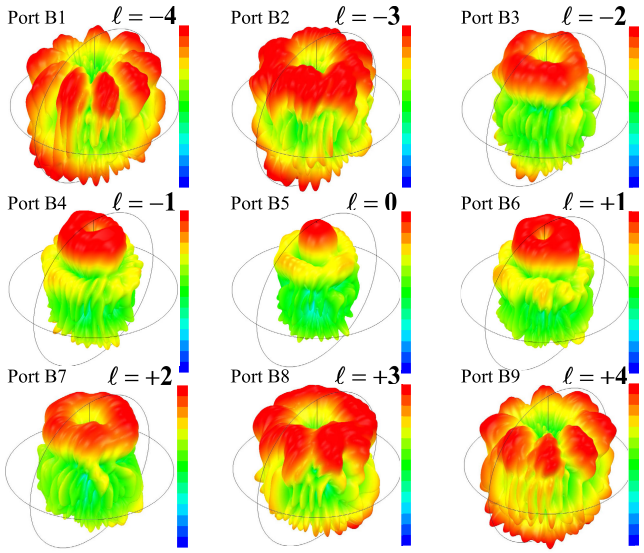

FIGURE 17. 3-D radiation patterns.

TABLE 5. Measured and simulated gains of the proposed antenna.

OAM mode	Proposed antenna		Ant 4
	measured (dBi)	simulated (dBi)	simulated (dBi)
$\ell = 0$	13.90	14.07	8.93
$\ell = \pm 1$	9.85	10.02	5.75
$\ell = \pm 2$	6.82	6.93	4.71
$\ell = \pm 3$	3.85	3.94	2.79
$\ell = \pm 4$	3.68	3.61	1.58

TABLE 6. Comparison with previous work.

Ref.	Antenna type	Planar structure	Feeding network	OAM modes
[18]	Circular array	Yes	Complex	±1
[19]	Circular array	Yes	Complex	+1/+2
[21]	Ring arrays with sequentially rotated configurations	Yes	Complex	+1/+2
[23]	Substrate integrated waveguide	Yes	No	±2/±6
[24]	Ring-slot with parabolic reflector	No	No	±2/±3
[26]	Flat dispersive metasurface	Yes	No	0/1/2
This work	Circular array	Yes	Rotman lens	0/±1/±2/ ±3/±4

quite aligned, which confirms that the proposed antenna can successfully generate nine different OAM modes in practice.

Fig. 16(a) shows the measured VSWR for each input port. Measured and simulated gains of the proposed antenna in different modes are given in Table 5. Compared with the simulated results of Ant 4 which uses a Rotman lens feeding nine convention microstrip antennas, the gains of the proposed antenna are significantly improved due to the adoption of high-gain antenna elements. Fig. 16 shows the measured and simulated radiation patterns of the proposed antenna. The simulated 3D radiation patterns are shown in Fig. 17.

The proposed antenna for multiple OAM modes is compared with several other works in Table 6. Obviously, the proposed antenna achieved the best in terms of OAM modes, which is very important to reap the potential of OAM-based communication for spectrum efficiency enhancement.

IV. CONCLUSION

This paper proposes an antenna design which utilizes a Rotman lens feeding a circular array to realize multiple OAM modes. The circular array element adopts a high-gain microstrip antenna, which significantly improves the gain of the proposed antenna. The method to improve the output amplitude of Rotman lens is investigated in detail so as to make each output port equal in amplitude. The experiment results via a prototype verified that nine different OAM modes can be generated but also OAM beam depression can be improved by the proposed design, which turns out to be a good enabler for an efficient OAM-based communication for spectrum efficiency enhancement.

REFERENCES

[1] S. M. Mohammadi, "Orbital angular momentum in radio—A system study," *IEEE Trans. Antennas Propag.*, vol. 58, no. 2, pp. 565–572, Feb. 2010.

[2] F. E. Mahmouli and S. D. Walker, "4-Gbps uncompressed video transmission over a 60-GHz orbital angular momentum wireless channel," *IEEE Wireless Commun. Lett.*, vol. 2, no. 2, pp. 223–226, Apr. 2013.

[3] L. Allen, M. W. Beijersbergen, R. J. Spreeuw, and J. P. Woerdman, "Orbital angular momentum of light and the transformation of Lagurre–Gaussian laser modes," *Phys. Rev. A, Gen. Phys.*, vol. 45, no. 11, pp. 8185–8189, 1992.

[4] F. Tamburini, E. Mari, B. Thidé, C. Barbieri, and F. Romanato, "Experimental verification of photon angular momentum and vorticity with radio techniques," *Appl. Phys. Lett.*, vol. 99, no. 20, Nov. 2011, Art. no. 204102.

[5] J. Wang, J.-Y. Yang, I. M. Fazal, N. Ahmed, Y. Yan, H. Huang, Y. Ren, Y. Yue, S. Dolinar, M. Tur, and A. E. Willner, "Terabit free-space data transmission employing orbital angular momentum multiplexing," *Nature Photon.*, vol. 6, no. 7, pp. 488–496, Jul. 2012.

[6] P. Schemmel, G. Pisano, and B. Maffei, "Modular spiral phase plate design for orbital angular momentum generation at millimeter wavelengths," *Opt. Express*, vol. 22, no. 12, pp. 14712–14726, Jun. 2014.

[7] X. Hui, S. Zheng, Y. Hu, C. Xu, X. Jin, H. Chi, and X. Zhang, "Ultralow reflectivity spiral phase plate for generation of millimeter-wave OAM beam," *IEEE Antennas Wireless Propag. Lett.*, vol. 14, pp. 966–969, 2015.

[8] W. Wei, K. Mahdjoubi, C. Brousseau, and O. Emile, "Horn antennas for generating radio waves bearing orbital angular momentum by using spiral phase plate," *IET Microw., Antennas Propag.*, vol. 10, no. 13, pp. 1420–1427, Oct. 2016.

[9] H.-F. Huang and S.-N. Li, "High-efficiency planar reflectarray with small-size for OAM generation at microwave range," *IEEE Antennas Wireless Propag. Lett.*, vol. 18, no. 3, pp. 432–436, Mar. 2019.

[10] S. Zheng, X. Hui, X. Jin, H. Chi, and X. Zhang, "Transmission characteristics of a twisted radio wave based on circular traveling-wave antenna," *IEEE Trans. Antennas Propag.*, vol. 63, no. 4, pp. 1530–1536, Apr. 2015.

[11] M. L. N. Chen, L. J. Jiang, and W. E. I. Sha, "Ultrathin complementary metasurface for orbital angular momentum generation at microwave frequencies," *IEEE Trans. Antennas Propag.*, vol. 65, no. 1, pp. 396–400, Jan. 2017.

[12] F. Qin, L. Wan, L. Li, H. Zhang, G. Wei, and S. Gao, "A transmission metasurface for generating OAM beams," *IEEE Antennas Wireless Propag. Lett.*, vol. 17, no. 10, pp. 1793–1796, Oct. 2018.

[13] B. Thidé, H. Then, J. Sjöholm, K. Palmer, J. E. S. Bergman, T. D. Carozzi, Y. N. Istomin, N. H. Ibragimov, and R. Khamitova, "Utilization of photon orbital angular momentum in the low-frequency radio domain," *Phys. Rev. Lett.*, vol. 99, no. 8, Aug. 2007, Art. no. 087701.

[14] A. Tennant and B. Allen, "Generation of OAM radio waves using circular time-switched array antenna," *Electron. Lett.*, vol. 48, no. 21, p. 1365, 2012.

[15] Q. Bai, A. Tennant, and B. Allen, "Experimental circular phased array for generating OAM radio beams," *Electron. Lett.*, vol. 50, no. 20, pp. 1414–1415, Sep. 2014.

[16] Y. Gong, R. Wang, Y. Deng, B. Zhang, N. Wang, N. Li, and P. Wang, "Generation and transmission of OAM-carrying vortex beams using circular antenna array," *IEEE Trans. Antennas Propag.*, vol. 65, no. 6, pp. 2940–2949, Jun. 2017.

[17] H. Li, L. Kang, F. Wei, Y.-M. Cai, and Y.-Z. Yin, "A low-profile dual-polarized microstrip antenna array for dual-mode OAM applications," *IEEE Antennas Wireless Propag. Lett.*, vol. 16, pp. 3022–3025, 2017.

[18] Y. Chen, X. Jin, H. Chi, X. Zhang, and S. Zheng, "Half-mode substrate integrated waveguide antenna for generating multiple orbital angular momentum modes," *Electron. Lett.*, vol. 52, no. 9, pp. 684–686, Apr. 2016.

[19] W. Zhang, S. Zheng, X. Hui, Y. Chen, X. Jin, H. Chi, and X. Zhang, "Four-OAM-mode antenna with traveling-wave ring-slot structure," *IEEE Antennas Wireless Propag. Lett.*, vol. 16, pp. 194–197, 2017.

[20] D. Weiguo, Z. Yongzhong, Y. Yang, and Z. Kaiwei, "A miniaturized dual-orbital-angular-momentum (OAM)-mode helix antenna," *IEEE Access*, vol. 6, pp. 57056–57060, 2018.

[21] Y. Zhang, Y. Lyu, H. Wang, X. Zhang, and X. Jin, "Transforming surface wave to propagating OAM vortex wave via flat dispersive metasurface in radio frequency," *IEEE Antennas Wireless Propag. Lett.*, vol. 17, no. 1, pp. 172–175, Jan. 2018.

[22] Z.-G. Guo and G.-M. Yang, "Radial uniform circular antenna array for dual-mode OAM communication," *IEEE Antennas Wireless Propag. Lett.*, vol. 16, pp. 404–407, 2017.

[23] D. Liu, L. Gui, Z. Zhang, H. Chen, G. Song, and T. Jiang, "Multiplexed OAM wave communication with two-OAM-mode antenna systems," *IEEE Access*, vol. 7, pp. 4160–4166, 2019.

[24] B. Liu, Y. Cui, and R. Li, "A broadband dual-polarized dual-OAM-mode antenna array for OAM communication," *IEEE Antennas Wireless Propag. Lett.*, vol. 16, pp. 744–747, 2017.

[25] Y.-M. Zhang and J.-L. Li, "Analyses and full-duplex applications of circularly polarized OAM arrays using sequentially rotated configuration," *IEEE Trans. Antennas Propag.*, vol. 66, no. 12, pp. 7010–7020, Dec. 2018.

[26] F. Qin, S. Gao, W.-C. Cheng, Y. Liu, H.-L. Zhang, and G. Wei, "A high-gain transmitarray for generating dual-mode OAM beams," *IEEE Access*, vol. 6, pp. 61006–61013, 2018.

[27] C. A. Balanis, *Antenna Theory: Analysis and Design*. Hoboken, NJ, USA: Wiley, 2005.

[28] X. Zhang and L. Zhu, "Gain-enhanced patch antenna without enlarged size via loading of slot and shorting pins," *IEEE Trans. Antennas Propag.*, vol. 65, no. 11, pp. 5702–5709, Nov. 2017.

[29] X. Y. Zhang, W. Duan, and Y.-M. Pan, "High-gain filtering patch antenna without extra circuit," *IEEE Trans. Antennas Propag.*, vol. 63, no. 12, pp. 5883–5888, Dec. 2015.

[30] X. Zhang and L. Zhu, "Gain-enhanced patch antennas with loading of shorting pins," *IEEE Trans. Antennas Propag.*, vol. 64, no. 8, pp. 3310–3318, Aug. 2016.

[31] M. S. M. Mollaei, E. Zanganeh, and M. F. Farahani, "Enhancement of patch antenna gain using cylindrical shell-shaped superstrate," *IEEE Antennas Wireless Propag. Lett.*, vol. 16, pp. 2570–2573, 2017.

[32] X. Zhang, L. Zhu, and Q.-S. Wu, "Sidelobe-reduced and gain-enhanced square patch antennas with adjustable beamwidth under TM_{03}Mode operation," *IEEE Trans. Antennas Propag.*, vol. AP-66, no. 4, pp. 1704–1713, Apr. 2018.

[33] X. Zhang, Q.-S. Wu, L. Zhu, G.-L. Huang, and T. Yuan, "Resonator-fed wideband and high-gain patch antenna with enhanced selectivity and reduced cross-polarization," *IEEE Access*, vol. 7, pp. 49918–49927, 2019.

[34] W. Rotman and R. Turner, "Wide-angle microwave lens for line source applications," *IEEE Trans. Antennas Propag.*, vol. 11, no. 6, pp. 623–632, Nov. 1963.

DAN WU was born in Chongqing, China, in 1991. He received the B.S. degree in electrical engineering from Xidian University, Xi'an, China, in 2014, where he is currently pursuing the Ph.D. degree. His current research interests include OAM waves and antenna arrays.

ZHIYA ZHANG was born in Jiangsu, China, in 1985. He received the B.S. degree in electrical engineering and the Ph.D. degree in electromagnetic field and microwave technology from Xidian University, Xi'an, China, in 2007 and 2012, respectively. He works as an Associate Professor with the Science and Technology on Antenna and Microwave Laboratory, Xidian University. His current research interests include broadband antennas, millimeter-wave antennas, and antenna arrays.

GUANG FU received the B.S. and M.S. degrees in electromagnetic field and microwave technology from Xidian University, in 1984 and 1991, respectively. He became a Professor with Xidian University, in 2001. His current research interests include theory and engineering of antennas and antenna arrays.

XIAOWEI SHI (Senior Member, IEEE) was born in Guangdong, China, in 1963. He received the B.S. degree in radio physics, the M.Eng. degree in electrical engineering, and the Ph.D. degree in electromagnetic field and microwave technology from Xidian University, Xi'an, China, in 1982, 1990, and 1995, respectively. From 1996 to 1997, he was a Cooperator with the Electronics and Telecommunications Research Institute, Daejeon, South Korea, for his Postdoctoral Research work. He is currently a Professor and an Advisor of Ph.D. degree students with Xidian University. His current research interests include the theory of microwave networks, microwave measurement, and electromagnetic inverse scattering, and the theory of electromagnetic variation, electromagnetic compatibility, and smart antennas.

LIN YANG received the B.S. and M.S. degrees in electromagnetic fields and microwave technology from Xidian University, Xi'an, China, in 1983 and 1994, respectively. He is currently a Professor with the National Key Laboratory of Antennas and Microwave Technology, Xidian University. He is also the Director of anechoic chamber with Xidian University.

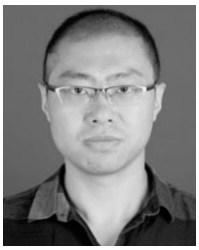

XI LI was born in Shaanxi, China, in 1983. He received the B.S. and Ph.D. degrees in electromagnetic field and microwave technology from Xidian University, Xi'an, China, in 2006 and 2011, respectively.

In 2011, he joined the National Laboratory of Science and Technology on Antennas and Microwaves, Xidian University, as an Associate Professor. He has authored or coauthored over 40 refereed journal and conference papers. His current research interests include antenna measurement theory, wideband antenna design, and rectenna design.